High-Resolution Snow Water Equivalent Estimation: A Data-Driven Method for Localized Downscaling of Climate Data

Fatemeh Zakeri [a,b], Gregoire Mariethoz [a], Manuela Girotto[b]

[a] Institute of Earth Surface Dynamics, Faculty of Geosciences and Environment, University of Lausanne, Lausanne,
5   Switzerland
[b] Department of Environmental Science, Policy, and Management, University of California, Berkeley, Berkeley, CA, USA

Correspondence to: Fatemeh Zakeri (fatemeh.zakeri@unil.ch; fatemeh.zakeri@berkeley.edu)

Abstract. Estimating high-resolution daily Snow Water Equivalent (SWE) in mountainous regions is challenging due to
10 geographical complexity and the irregular availability of high-resolution meteorological data. This study introduces a method
for downscaling SWE. It is based on the dependence between meteorological estimators and SWE, and the fact that while
SWE can change rapidly within days, its patterns may exhibit year-to-year analogies under similar meteorological conditions.
We implement this principle to downscale SWE to a 500 m resolution using a K-nearest neighbor algorithm with a customized
distance metric.

15 To evaluate the performance of our approach, we conduct tests in two regions of interest in the western United States. A cross-
validation analysis is performed, and comparisons are made with commonly used SWE datasets as well as against in-situ data.
The results demonstrate that our approach enables the generation of downscaled SWE that closely matches that observed in
reanalysis data in terms of statistical properties. This opens up possibilities for applications in regions with limited in-situ data
or meteorological data. The approach also has the potential to recreate unmeasured historical SWE values and could be
20 extended to future periods using climate projections.

Keywords: Downscaling; Climate Reanalysis; Time Series; Snow Eater equivalent; K-Nearest Neighbors; Data-Driven
Method; Spatial and Temporal Analysis

1. Introduction

The snowpack in high-elevation regions plays a crucial role as a primary source of streamflow, particularly during the spring
25 and summer seasons (Bales et al., 2006). Rapidly changing weather conditions (Ranzi et al., 2024) and extreme events, such
as atmospheric rivers, can lead to significant snowmelt and generate extreme runoff, posing threats to both water supply and
infrastructure (Henn et al., 2020). Understanding snow and its role in the hydrological cycle is not merely a scientific question,
but also a matter of economic significance as it directly relates to water resources, agriculture, and energy production (Sturm

et al., 2017). Therefore, accurate and detailed information on Snow Water Equivalent (SWE) with high temporal and spatial

30   resolution is crucial for effective water resource management and decision-making (Bales et al., 2006).

Although ground stations are valuable for collecting SWE data, their limited presence in certain regions affects their representativeness. Furthermore, variations in topography, land cover, and environmental conditions in mountainous areas make point-scale data insufficient for capturing the overall spatial scale of a watershed (Bales et al., 2006). To mitigate this lack of data, physically based snow models use an energy balance approach to estimate snowmelt. Various models of different

35   complexities have been introduced, but complex models often require extensive data that may not be readily accessible, while simpler models may not fully capture the complexity of the snowmelt process (Bair et al., 2016; Clow et al., 2012). Moreover, to achieve high-resolution SWE estimates using these models, it is necessary to use meteorological and land cover-related data that matches the desired output resolution of the SWE. However, obtaining high-resolution data in mountainous regions remains challenging (Wundram and Löffler, 2008).

40   Reflecting on these challenges in obtaining high-resolution climate data, remote sensing is becoming increasingly important for monitoring and predicting snowpack conditions and their impacts on water resources ((Usbr), 2021). Satellites equipped with optical sensors such as MODIS and Landsat provide data on snow cover (Dietz et al., 2012; Painter et al., 2012; Largeron et al., 2020; Wu et al., 2021) and temperature (Lundquist et al., 2018), while lidar and microwave sensors (Tsang et al., 2021; Saberi et al., 2020) offer insights into snow depth or SWE (Lievens et al., 2019; Shi and Dozier, 2000; Pflug et al., 2024; Ma

45   et al., 2023) and wetness (Shi and Dozier, 1995; Snapir et al., 2019). However, limitations such as revisit time and cloud cover restrict the availability of daily data.

To overcome the limitations of models and observations, data assimilation has emerged as a promising approach because it capitalizes on the strengths of both observations and models, minimizing their respective uncertainties. It has proven useful in improving the accuracy of snow state estimates, snow physics, model parameters, and identifying sources of uncertainty. Data

50   assimilation is particularly effective in harmonizing the different temporal and spatial resolutions of in-situ and remotely sensed observations and bridging the scale gap between observations and models. In general, the assimilation of satellite and airborne observations leads to enhanced estimates of seasonal snow and related variables (Fang et al., 2022; Margulis et al., 2016). However, snow data assimilation has its shortcomings, the largest one being that it cannot provide daily high-resolution SWE (HR-SWE) for periods when no satellite data are available. Key areas of ongoing research include understanding the impact

55   of underlying spatial error correlations in data assimilation to improve the spatial estimates of SWE, and the potential integration of multiple observations to boost snow model accuracy. Despite these challenges, the snow science community continues to make strides in enhancing the accuracy of seasonal snow estimation (Girotto et al., 2020).

Acknowledging the complexities involved in modeling snow processes and assimilating diverse datasets, we propose a localized climate data downscaling method to estimate HR-SWE. Statistical downscaling methods have demonstrated their

60   capability to act as a bridge between large-scale climate forecasts and local-scale climate impacts (Abatzoglou and Brown, 2012; Tabari et al., 2021; Rettie et al., 2023). Recognizing the potential for snow patterns to repeat in years with similar climate

characteristics (Zakeri and Mariethoz, 2024; Pflug and Lundquist, 2020), this study aims to provide daily, high-spatial-resolution SWE data. Our proposed approach is based on establishing a statistical relationship between daily global low-resolution climate data, such as temperature, precipitation, low-resolution SWE (LR-SWE), and local reanalysis HR-SWE

65 images as a training dataset. Then, based on this learned relationship, embedded in a K-nearest neighbor algorithm, a unique daily HR-SWE dataset is obtained for the historical period (1950 to present) based on low-resolution climate data. The paper is structured as follows: Section 2 details the methodology; Section 3 describes the study area, database, and parameters; Sections 4 and 5 present the evaluation approaches and the results; and Section 5 concludes with discussions and conclusions.

2. Methodology

70 ### 2.1 Overview of the Algorithm

The algorithm involves two primary datasets: the training dataset and the target dataset. The training dataset consists of HR-SWE images and low-resolution (LR) climate data. In contrast, the target dataset includes LR-SWE images alongside LR climate data, for which we aim to estimate HR-SWE images.

The fundamental strategy of the proposed method involves ranking the data in the training dataset to estimate an HR-SWE

75 image for a given target date. This ranking is based on the Manhattan distance between each date in the training dataset and the selected target date, as detailed in Section 2.3. The Manhattan distance is chosen as it is more robust against outliers and often computationally cheaper than the Euclidean distance. Then, the algorithm estimates the downscaled SWE for the target date based on the K-nearest SWE candidates. As detailed in the recent work by Zakeri and Mariethoz (2024), this approach was initially designed to create synthetic satellite snow cover images for dates with no satellite data, based on the relationship

80 between meteorological estimators from the ERA5-Land reanalysis dataset and available clear sky Landsat/Sentinel-2 snow cover images. Here, we have adapted this approach to downscale SWE. The innovation lies in the focus on downscaling the LR daily SWE data at the spatial scale of climate model simulations to produce much higher-resolution daily SWE estimates. This output is particularly important in areas with complex terrain, such as the Western United States, where global models face challenges in accurately representing the regional climate. Indeed, the resolution of global climate simulations is often

85 insufficient for capturing local influences (e.g., topography or vegetation) on SWE patterns. On the other hand, physical models are computationally expensive. Therefore, developing a tool to estimate HR-SWE that closely aligns with established regional HR-SWE reanalysis is essential for scientific and management purposes, offering a faster and less computationally demanding solution. Further details of the proposed methodology will be provided in the subsequent sections.

2.2 Input Data and Preprocessing

2.2.1 Definition of Temporal Intervals for Climate Variables

SWE, representing the amount of water stored in the snowpack, is influenced by various factors, which can be classified into two main categories: climatic variables (such as temperature, precipitation, and surface downwelling shortwave radiation) and environmental variables (including land cover, topography, and the presence of topography shadows). While environmental variables can impact SWE distribution and accumulation, their effects are assumed to be consistent and not subject to significant temporal variations within the specified regions. Therefore, for downscaled SWE estimation, we primarily focus on climatic variables and do not explicitly incorporate topography and land cover information.

SWE is also affected by conditions in the preceding periods. To represent this, we introduce two distinct climate temporal intervals: a near interval and a far interval (refer to Fig. 1). These intervals consider climate variables such as minimum temperature, maximum temperature, precipitation, and surface downwelling shortwave radiation. Considering both far and near-term variations allows accounting for complex relationships between the climate dynamics and snow accumulation and melting. By incorporating these intervals, we can capture the influence of climate variables over different timescales and improve the accuracy of SWE estimation. The specific lengths of these far and near climate intervals are determined through an optimization procedure outlined in Section 2.4.1.
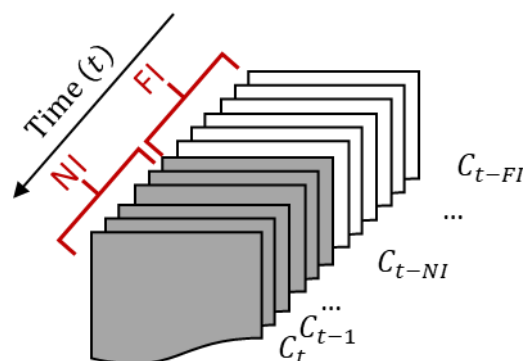

Fig. 1. Illustration of the definition of Near (shown in gray) and Far (shown in white) daily intervals for climate variables, highlighting the Far Temporal Interval (FI) and Near Temporal Interval (NI) of Climate Data at a Specific Time (C_t).

2.2.2 Input Climate Variables

The downscaling process relies on low-resolution climate information and LR-SWE data obtained from global or regional climate models. As a result, the SWE downscaling procedure can be described by Equation (1):

$$S\widehat{WE}_{HR}(t) \approx f(T_{min,LR}^{FI}, T_{min,LR}^{NI}, T_{max,LR}^{FI}, T_{max,LR}^{NI}, P_{LR}^{FI}, P_{LR}^{NI}, RSDS_{LR}^{FI}, RSDS_{LR}^{NI}, SWE_{LR}(t)) \tag{1}$$

Here, $S\widehat{WE}_{HR}(t)$ and $SWE_{LR\ (t)}$ are the downscaled SWE and the LR-SWE, both at the query time (t), and T_{min} and T_{max} represent the minimum and maximum temperature, while *P* and *RSDS* denote precipitation and surface downwelling shortwave

110 radiation. The superscript $"^{FI}"$ or $"^{NI}"$ indicates the far or near temporal intervals that are introduced in Fig. 1. The subscript notation $("_{LR}","_{HR}")$ explicitly indicates the resolution (Low Resolution, High Resolution). All climate variables (T_{min}, T_{max}, P, RSDS, SWE) are daily measurements. To ensure compatibility among datasets with varying units, all input data are rescaled to a range of 0-1 based on the absolute minimum and maximum values observed in the training dates. Hereafter, SŴE refer to downscaled SWE.

2.3 Downscaled SWE Estimation

Estimating SŴE for a date when it is not available relies on the existing HR-SWE data from the training dates. The training dates consist of the input variables described in Equation (1) and their corresponding HR-SWE images. By utilizing a vector of inputs, we estimate SŴE by selecting the K-nearest candidates in the input space. The downscaling process follows these steps:

120   1.   Gather the input variables, including the far and near intervals of temperature, precipitation, shortwave radiation, and the LR-SWE for both the target date and the training dates.

    2.   Calculate the similarity or distance between the input vector of the target date and the input vectors of the training dates.

    3.   Select the K-nearest training dates based on their proximity to the target date in the input space.

125   4.   Retrieve the corresponding HR-SWE images associated with the selected K-nearest training dates.

    5.   Aggregate the retrieved HR-SWE images to estimate SŴE for the target date.

The metric used to identify the nearest neighbors between a given target date (t_1) and a training date (t_2) is the multivariate Manhattan distance, described in Equation (2):

$$d\{t_1, t_2\} = \sum_{i=1}^{E} \alpha_i |x_i(t_2) - x_i(t_1)| \tag{2}$$

The weights α_i assigned to the input variables add up to 1 and are used to balance their influence in the selection of the K-

130 nearest observations. The determination of optimal weights is further discussed in Section 2.4.2. Here, x_i represent each of the *E* estimators introduced in Equation (1).

2.4 Estimating Parameters and Weights

To optimize parameter estimation and ensure better convergence, the parameters are estimated either using sensitivity analysis or an optimization algorithm. In this paper, the determination of the far and near intervals (FI and NI) for climate variables
135 (Fig. 1), as well as the number of K-nearest observations, are achieved through a sensitivity analysis. The weights assigned to the input features are established using an optimization algorithm.

2.4.1 Parameter Sensitivity Analysis

The measure of dissimilarity, denoted as ε, is critical for determining the optimal near (NI) and far (FI) temporal intervals, as well as the optimal number of nearest observations (K), for estimating $S\hat{W}E$. This dissimilarity is quantified using the Root-
140 Mean-Squared Error (RMSE), a standard measure of accuracy that reflects the average magnitude of the square of errors between estimated and observed values. The RMSE is defined as follows:

$$RMSE = \sqrt{\frac{\sum_{i=1}^{N}\left(S\hat{W}E_i - SWE_i\right)^2}{N}} \tag{3}$$

where $S\hat{W}E_i$ is the downscaled SWE at the ith pixel, SWE_i is the observed (reference) HR-SWE at the ith pixel, and N is the total number of pixels. This formula underpins the evaluation of ε across different configurations of temporal intervals and K-
145 nearest observation counts.

To identify the optimal temporal intervals (NI^* and FI^*), we conduct a sensitivity analysis within predefined ranges, set by $NI \in [1,7]$; and $FI \in [1,90]$, aiming to minimize ε. Similarly, the optimal number of nearest observations (K^*) is determined by evaluating ε as a function of K, within a range 1 to the maximum number of available training dates ($K \in [1, K_{max}]$) to identify the configuration that yields the smallest dissimilarity between $S\hat{W}E$ and reference HR-SWE. The maximum number
150 of available training dates (K_{max}) can vary for each case study from several days to several months.

Mathematically, the optimization processes are represented as:

$$NI^* = \underset{NI}{\operatorname{argmin}}\ \varepsilon_{NI}$$
$$FI^* = \underset{FI}{\operatorname{argmin}}\ \varepsilon_{FI} \tag{4}$$
$$K^* = \underset{K}{\operatorname{argmin}}\ \varepsilon_{K}$$

where ε_{FI}, ε_{NI}, and ε_K are the sum of RMSEs for respective configurations, reflecting the dissimilarity between $S\hat{W}E$ (using different sizes of NI, FI, and K) and the reference HR-SWE. The only distinction between $RMSE_{FI}$, $RMSE_{NI}$, and $RMSE_K$ is based on the varying elements (FI, NI, or K), illustrating how each influences the $S\hat{W}E$ estimate. The determination of these
155 optimal parameters enables the refinement of our SWE estimation model, enhancing its accuracy by minimizing ε.

2.4.2 Weights Optimization

The weights α_i defined in Equation (2) are determined by minimizing the RMSE between the $\hat{SWE}$ and the reference HR-SWE using Bayesian optimization. In this model-based optimization, the global maximum or minimum of an unknown objective function is found sequentially (Shahriari et al., 2015; Snoek et al., 2012). The key aspect of this approach is the use

160 of a probabilistic model of the response function, which is evaluated at a minimal cost through the acquisition function. The Bayesian optimization framework employs a Gaussian process prior over the objective function and iteratively refines the model through Bayesian posterior updating to determine the optimal solution.

3. Study Areas, Datasets, and Parameters

3.1 Study Areas

165 To evaluate the effectiveness of the proposed methodology, we selected two regions in the Western United States as indicated in Figure 2: the California Sierra Nevada region (referred to as California) and the Upper Colorado River basin (referred to as Colorado). These regions heavily rely on snowmelt as a vital source of water resources (Dawadi and Ahmad, 2012; Siirila-Woodburn et al., 2021).

(a) Western U.S.
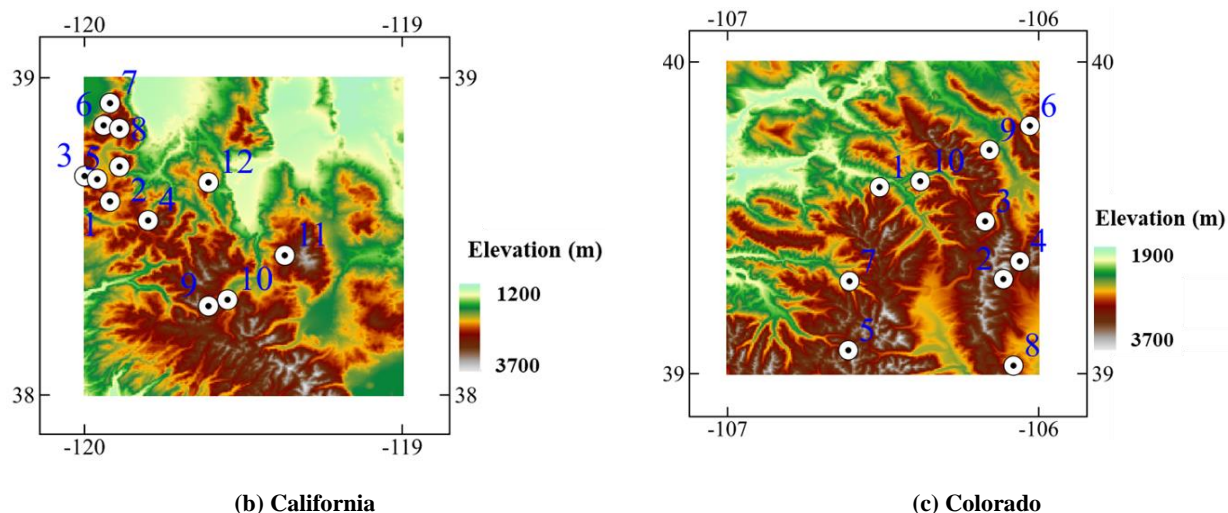
(b) California **(c) Colorado**
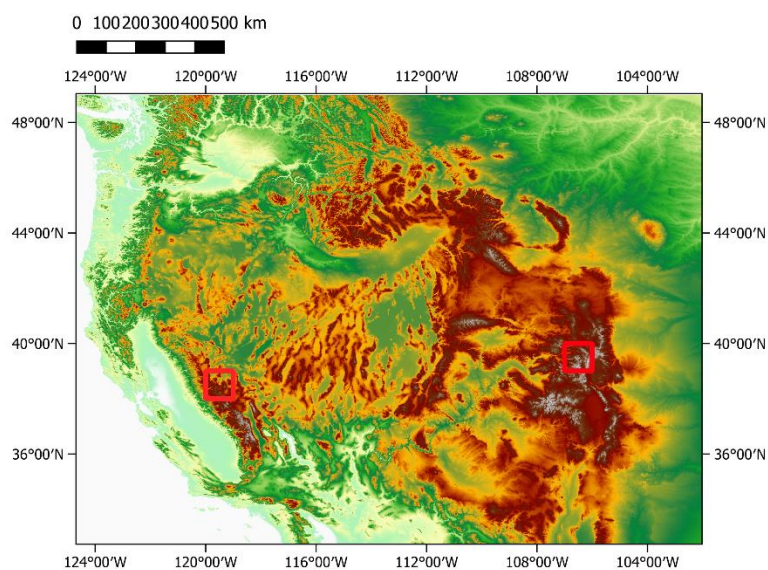
Fig. 2. a) Map of elevation (in meters) across the Western United States, highlighting two regions of interest (red squares). b) Map of elevation and locations of in-situ sites in the Sierra Nevada, California .c) Map of elevation and locations of in-situ sites in the Upper Colorado River basin, Colorado.

In the California region, elevation ranges from a minimum of 1200 m to a maximum of 3700 m, with an average elevation of
170   2200 m. In the Colorado region, elevation ranges from a minimum of 1900 m to a maximum of 4300 m, with an average elevation of 3000 m. By focusing on these specific regions, we can assess the performance and applicability of the proposed methodology in other areas where snow water resources are an important component of the hydrology.

3.2 Datasets

The reference high-resolution SWE data, which this study aims to produce, is sourced from the reanalyzed SWE dataset for
175   the Western United States (Fang et al., 2022). This dataset, captured at a 16 arcsecond (~500 m) resolution, covers the period from the water year (i.e., 1st October to 30th September) 1984 to 2021 and is updated daily. It offers ensemble median values of SWE, calculated from a discrete probability distribution of posterior weights, thus providing an extensive and detailed view of the snow water content over the years. The dataset can be accessed at https://doi.org/10.5067/PP7T2GBI52I2. Hereafter, we refer to this dataset as the UCLA SWE.

180   To obtain the necessary climatic estimators, such as daily minimum and maximum air temperature, daily total precipitation, and shortwave radiation, we utilize two distinct sources: the Coupled Model Intercomparison Project (CMIP) version 6 simulations (Meehl et al., 2014) and the downscaled CMIP6 over the Western United States using the Weather Research and Forecasting (WRF) model datasets (referred to as WRF-CMIP6) (Rahimi et al., 2024; Rahimi et al., 2022). The CMIP6 simulations provide daily climate data at a spatial resolution of 100 km, while the WRF-CMIP6 datasets offer high-resolution
185   daily climate simulations at a resolution of 9 km for the Western United States.

Rahimi et al. (2024) created climate data utilizing reanalysis data based on dynamical downscaling to refine global climate models through regional climate models, specifically using the WRF model. They used ERA5 reanalysis data for calibrating and validating the WRF model setup. This method effectively enhances the representation of local weather phenomena by increasing resolution, thereby improving the accuracy of climate projections, particularly in areas with complex terrain like the Western United States.

While CMIP6 models capture long-term climate variability and trends, including seasonality that might influence snow patterns, their resolution is relatively coarse. In other words, they simulate the general variability and stochastic nature of the climate. However, WRF-CMIP6 incorporates ERA5 reanalysis data in the process of dynamically downscaling CMIP6 data, using a configuration that also considers temporal and spatial variability in the selection of global climate models for the Western United States. This results in more accurate regional climate models. Utilizing both CMIP6 and WRF-CMIP6 at different resolutions enables us to investigate the impact of using a regional configuration of a climate model that dynamically downscales CMIP6 data, incorporating reanalysis data, alongside a global climate model with different spatial resolutions on the accuracy of our approach.

To illustrate the effect of resolution on the accuracy of the SWE image, Fig. 3 depicts the UCLA SWE, WRF-CMIP6, and CMIP6 images for a day in the California region.
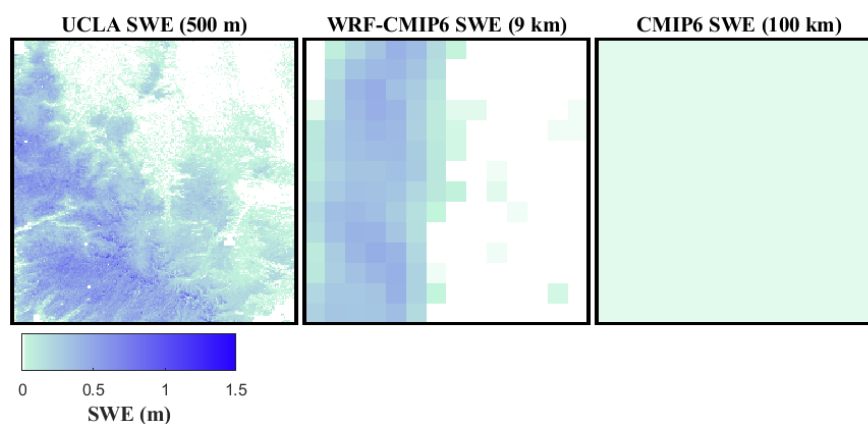

Fig. 3. Comparative illustration of SWE images highlighting the effect of spatial resolution on accuracy. Displayed from left to right are the UCLA SWE, WRF-CMIP6, and CMIP6 images captured over the California region (Fig. 2 (b), lon:-120 to -119, lat: 38 to 39) on January 8, 1995. The distinct variations between these images underscore the influence of scaling on image accuracy.

Among the available models with resolutions of both 9 km and 100 km, we have selected three models for testing our methodology (Table 1). These models have been utilized in other studies (Thrasher et al., 2022; Kouki et al., 2022); although our methodology is not limited to these models, they were selected merely as examples. Hereafter, we will refer to them as 'cnrm-esm2-1', 'ec-earth3-veg', and 'mpi-esm1-2'.

205

Table 1. The climate models that are used in this study.

Climate model	Developer	100 km resolution	9 km resolution
cnrm-esm2-1	The Earth system model of CNRM of 2nd generation was developed by the CNRM/CERFACS.	CMIP6 data: https://esgf-node.ipsl.upmc.fr/search/cmip6-ipsl/;	WRF-CMIP6 data: https://registry.opendata.aws/wrf-cmip6/;
ec-earth3-veg	A configuration extending the Earth System Model EC-Earth3 developed by the EC-Earth Consortium.		
mpi-esm1-2-lr	Part of the family of Earth System Models (ESMs) developed by the Max Planck Institute (MPI).	Historical period (1985-2014) downloaded in January 2023.	Historical period (1985-2014) downloaded in January 2023.

To ensure that the test dates are not influenced by the training dates, the periods 1985-2004 and 2011-2014 are designated as training dates, while the years 2005 to 2010 are allocated for testing. Additionally, to confirm that our testing dates are not grouped into nearly identical wet or dry categories, we employed the CONUS Drought Indices dataset (Abatzoglou, 2013).

210 This dataset includes drought indices derived from the 4-km daily Gridded Surface Meteorological (GRIDMET) dataset. The Standardized Precipitation Evapotranspiration Index (SPEI) is the specific drought index used in our analysis. We calculated the average aggregated SPEI for each year across each region to categorize the testing and training years in Supplementary Table S1. As is clear, the testing years are different in terms of the drought index.

3.3 Parameters for Both Case Studies

215 Through a sensitivity analysis, we determine the NI^* and FI^* using Equation (4). This analysis is carried out for both datasets: CMIP6 (100 km) and WRF-CMIP6 (9 km). The results of this analysis are presented in supplementary Figures S1 to S4, indicating that a FI^* of 60 days and a NI^* of 4 days are sufficient for accurate SWE estimation in all examined scenarios. Even though these values might not represent a global optimum, potential suboptimal effects are deemed negligible. Furthermore, these effects are addressed in subsequent optimization stages when determining weights.

220 Next, we conduct a sensitivity analysis for the parameter K^*, the number of nearest observations, using the methodology described in Section 2.4.1 and Equation (4). Fig. S5 and Fig. S6 illustrate that, on average, a value of K^*=130 is appropriate for both the California and Colorado regions. Considering the relatively small variations in accuracy, we decided not to optimize K for each dataset. Note that the value of 130 nearest observations is high. This suggests the presence of frequently repeating situations or patterns within the dataset. This is advantageous for statistical analysis, as it provides a substantial

225 volume of data points, thereby enhancing the robustness and reliability of our statistical inferences.

The optimized weights α obtained from the Bayesian optimization algorithm after 500 iterations are summarized in Table 2. Similar weight patterns are observed in both regions. In general, relatively high weights are assigned to variables $T^{NI}_{min,LR}$, P^{NI}_{LR}, SWE_{LR}, and P^{FI}_{LR}.

Table 2. Weight optimization (α, in Equation (2)) results using Bayesian optimization. The numbers greater than 0.1 are bolded. This value, 0.1, is chosen because it almost represents the scenario where weights are distributed equally. cnrm refers to 'cnrm-esm2-1', earth3 to 'ec-earth3-veg', and mpi to 'mpi-esm1-2'.

Region of Interests	California						Colorado					
Climate Model	cnrm		earth3		mpi		cnrm		earth3		mpi	
Climate resolution (km)	**100**	**9**	**100**	**9**	**100**	**9**	**100**	**9**	**100**	**9**	**100**	**9**
$T^{NI}_{max,LR}$	0.03	0.08	**0.24**	**0.12**	**0.12**	**0.17**	0.03	0.02	0.01	**0.21**	0.01	**0.24**
$T^{NI}_{min,LR}$	**0.16**	0.08	**0.13**	0.03	0.08	**0.10**	**0.10**	**0.13**	**0.18**	**0.35**	**0.18**	**0.15**
P^{NI}_{LR}	**0.27**	0.04	**0.15**	**0.21**	**0.15**	**0.15**	**0.24**	**0.14**	**0.32**	0.04	**0.33**	0.09
$RSDS^{NI}_{LR}$	0.03	0.05	0.04	**0.13**	0.04	0.02	**0.25**	0	0	0.01	0	0
$T^{FI}_{max,LR}$	0.03	0.03	**0.15**	0.02	**0.27**	**0.17**	0	0.02	0.01	0.01	0.01	0.08
$T^{FI}_{min,LR}$	0.03	0.05	0.04	0.03	0.03	**0.18**	0	**0.31**	0	0.01	0	**0.33**
P^{FI}_{LR}	**0.27**	**0.31**	0.03	**0.19**	0.03	**0.13**	0.01	**0.36**	**0.33**	**0.26**	**0.32**	0
$RSDS^{FI}_{LR}$	0.03	0.04	**0.11**	**0.20**	0.03	0.02	**0.30**	0	0	0	0	0
SWE_{LR}	**0.14**	**0.32**	**0.11**	0.07	**0.25**	0.07	0.07	0	**0.15**	**0.10**	**0.15**	**0.11**

4. Evaluation Approach

230 Our method is evaluated through various accuracy metrics and independent datasets. Firstly, we generate two quality metrics in conjunction with the SŴE images. These metrics provide a quick assessment of the quality of the SŴE products. For each target date, two quality metrics are provided: the average and the standard deviation of the similarity metric across the K best-selected SWE candidates. The lower the average and standard deviation of the similarity metric, the better the SŴE estimation.

4.1 Time-Series Visualization

235 To further demonstrate the efficacy of our method, we showcase some SWE time series spanning six years at in-situ locations that are obtained from the Snow Telemetry (SNOTEL) network (https://www.wcc.nrcs.usda.gov/snow/). First, the pixels nearest to the in-situ locations are identified. Then, the SWE values at these locations in both the UCLA SWE data and other well-established SWE datasets (explained in Section 4.3) in the Western United States are compared with the SŴE values at these locations. We also present scatter plots colored by density (density scatter plots) illustrating the correlation between

240 reference (UCLA SWE) and SŴE values at in-situ locations. As in Fang et al. (2022)'s study, SWE values below 1 cm are excluded from the comparison. This screening is done because very small SWE values (less than 1 cm) can be the result of measurement errors, minimal snow presence, or other factors that might not provide meaningful data.

4.2 Cross-validation

We also validate our results using cross-validation. This involves removing six years of the UCLA SWE from the training
245 dataset. Then, we estimate $\hat{SWE}$ based on the remaining training data and compare the results with the reference UCLA SWE
image using correlation, mean difference, and RMSE as evaluation criteria. These assessment metrics are summarized in Table
3.

Table 3. A summary of accuracy assessment criteria.

Mean difference	A lower value indicates a better estimation	$MD=Mean(SWE-\hat{SWE})$
Correlation	A higher value indicates a better estimation	$R=\dfrac{\sum_{i=1}^{N}\left(\hat{SWE}_i-\overline{\hat{SWE}}\right)(SWE_i-\overline{SWE})}{\sqrt{\left(\sum_{i=1}^{N}\left(\hat{SWE}_i-\overline{\hat{SWE}}\right)^2\right)\left(\sum_{i=1}^{N}(SWE_i-\overline{SWE})^2\right)}}$
RMSE	A lower value indicates a better estimation	Equation (3)

where $\hat{SWE}_i$ is the downscaled SWE at the ith pixel, SWE_i is the observed (reference) SWE at the ith pixel, and N is the total
250 number of pixels.

In our quantitative comparison, we calculate the accuracy metrics at different elevation bands (elevation < 2000 m, 2000 m <
elevation < 3000 m, and elevation > 3000 m) and across various land cover types, including forest and non-forest areas. We
utilize the MODIS Land Cover Type (MCD12Q1) Version 6.1 data for land cover information (https://lpdaac.usgs.gov). This
data, as of 2018, is maintained by the NASA EOSDIS Land Processes Distributed Active Archive Center (LP DAAC) at the
255 USGS Earth Resources Observation and Science (EROS) Center in Sioux Falls, South Dakota. Elevations are derived from
the NASA SRTM Digital Elevation 30 m data (Farr et al., 2007).

4.3 Comparison with Independent SWE Datasets

To enhance the reliability of the $\hat{SWE}$, additional verification is performed through comparisons with the three following
independent SWE datasets. These comparisons are essential for validating the accuracy and consistency of our $\hat{SWE}$ images,
260 using the rigorous evaluation criteria detailed in Table 3.

SNODAS 1 km SWE Product

The first independent dataset includes the 1 km SWE data from the Snow Data Assimilation System (SNODAS), developed
by the NOAA National Weather Service's National Operational Hydrologic Remote Sensing Center (NOHRSC) (Center,
265 2004). SNODAS is a comprehensive modeling and data assimilation system designed to provide estimates of snow cover,
which are crucial for hydrologic modeling and analysis. The dataset covers the period from September 28, 2003, to the present.

12

We first resample the SŴE images by aggregating the values of all pixels that intersect each 1 km SNODAS pixel. This ensures that both datasets have the same spatial resolution. Subsequently, we compare the SNODAS SWE products with the SŴE images using the evaluation criteria introduced in Table 1. SWE pixel values less than 1 cm are not included in the comparison.

270

Daymet 1 km SWE Product

The second independent dataset includes the 1 km SWE data from the Daymet V4 dataset: Daily Surface Weather and Climatological Summaries (Thornton et al., 2022). Daymet provides gridded estimates of daily weather parameters for North America, including minimum and maximum temperatures, precipitation, and SWE, with data spanning from January 1, 1980.

275 We follow a similar procedure as in the comparison with the SNODAS SWE products.

University of Arizona (UA) 4 km SWE Product

The first independent dataset is the 4 km SWE data provided by the University of Arizona (UA) (Broxton et al., 2019; Zeng et al., 2018). It assimilates in-situ snow measurements from the SNOTEL and Cooperative Observer Network (COOP)

280 networks (Fleming et al., 2023; Council and Committee, 1998), incorporating detailed snow data. It also integrates modeled, gridded temperature and precipitation data, ensuring a comprehensive representation of SWE over the conterminous United States since 1981. For this comparison, we employ a similar procedure as in the comparisons with the previous two independent SWE products.

5. Results

285 **5.1 Time-Series Visualizations**

To showcase the effectiveness of the proposed technique, SWE time series that encompass a six-year duration at the three highest elevation in-situ locations (see Table 4) in California are presented in Fig. 4 (and Supplementary Fig. S7 for Colorado). These time series visually represent the SŴE values over time, enabling a comparison between the SŴE values, and the UCLA SWE, Daymet, SNODAS, and UA SWE data. The red line, representing our estimation, generally tracks the blue line (UCLA

290 SWE) well across the six-year period for the three high-elevation locations. However, in some years and locations, such as at the 'Leavitt Lake' and 'Lobdell Lake' stations in 2005, the red line diverges slightly from the blue line, indicating variability in estimation accuracy across different time periods. Nevertheless, even in 2005, our estimation is still within the range of other well-established SWE estimations. Moreover, in 2005, the other datasets also do not agree on the amount of SWE, indicating that this year is intrinsically challenging. This demonstrates that the proposed method can closely estimate the UCLA SWE at

295 a point scale in most years.

Table 4. Names and locations of in-situ sites.

	California				Colorado		
Station Name	Elevation (m)	Lat	Lon	Station Name	Elevation (m)	Lat	Lon
1. 'Blue Lakes'	2438	38.61	-119.92	1. 'Beaver Ck Village'	2612	39.60	-106.51
2. 'Burnside Lake'	2478	38.72	-119.89	2. 'Buckskin Joe'	3404	39.30	-106.11
3. 'Carson Pass'	2547	38.69	-120.00	3. 'Copper Mountain'	3207	39.49	-106.17
4. 'Ebbetts Pass'	2639	38.55	-119.80	4. 'Hoosier Pass'	3539	39.36	-106.06
5. 'Forestdale Creek'	2441	38.68	-119.96	5. 'Independence Pass'	3230	39.08	-106.61
6. 'Hagans Meadow'	2360	38.85	-119.94	6. 'Middle Fork Camp'	2734	39.80	-106.03
7. 'Heavenly Valley'	2601	38.92	-119.92	7. 'Nast Lake	2660	39.30	-106.61
8. 'Horse Meadow'	2607	38.84	-119.89	8. 'Rough And Tumble'	3179	39.03	-106.08
9. 'Leavitt Lake'	2927	38.28	-119.61	9. 'Summit Ranch'	2856	39.72	-106.16
10. 'Leavitt Meadows'	2195	38.30	-119.55	10. 'Vail Mountain'	3142	39.62	-106.38
11. 'Lobdell Lake'	2820	38.44	-119.37				
12. 'Monitor Pass'	2533	38.67	-119.61				
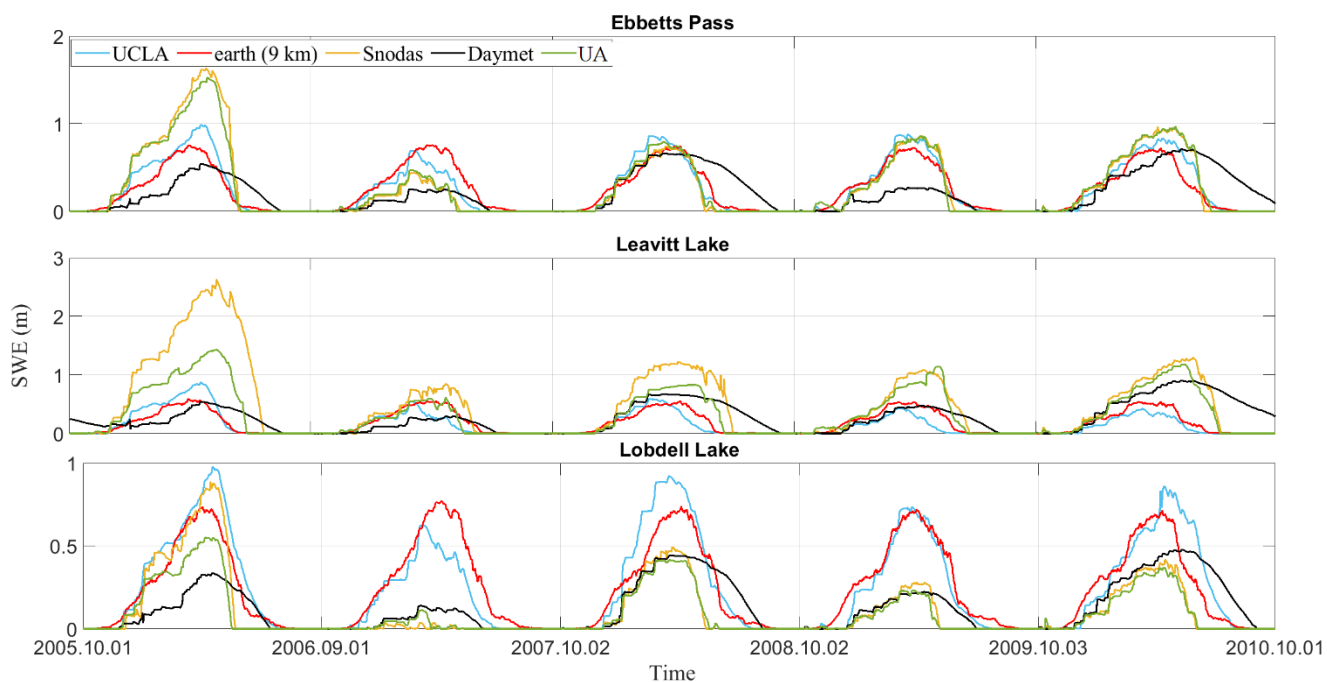
Fig. 4. The SWE time series spans a six-year period at the three highest elevations in-situ locations (Table 4) in California. "UA" represents the University of Arizona SWE datasets. The downscaled SWE (SŴE) results were obtained from the 'ec-earth3-veg' climate data at a 9 km resolution.

Additionally, density scatter plots are obtained using the 'dscatter' function (Henson, 2024) and are illustrated in Fig. 5 for California (and Supplementary Fig. S8 for Colorado), depicting the relationship between UCLA SWE and SŴE values at in-

300   situ locations (see Table 4) obtained from three climate models as estimators: 'ec-earth3-veg', 'mpi-esm1-2', and 'cnrm-esm2-1' at both 9 km and 100 km resolution.

Referencing Fig. 5, using 'ec-earth3-veg' at a 9 km resolution as an estimator, the derived SŴE in California shows a stronger correlation with the UCLA SWE at in-situ locations, achieving an R-value of approximately 0.87. This model also demonstrates improved accuracy, with a lower RMSE and MD (approximately 0.14 (m) for RMSE and about 0.02 (m) for

305   MD). In contrast, as shown in Supplementary Fig. S8, using 'cnrm-esm2-1' at a 100 km resolution as an estimator, the derived SŴE in Colorado exhibits a stronger correlation with the UCLA SWE at in-situ locations, marked by an R-value close to 0.85, and the RMSE estimated at around 0.09 m.
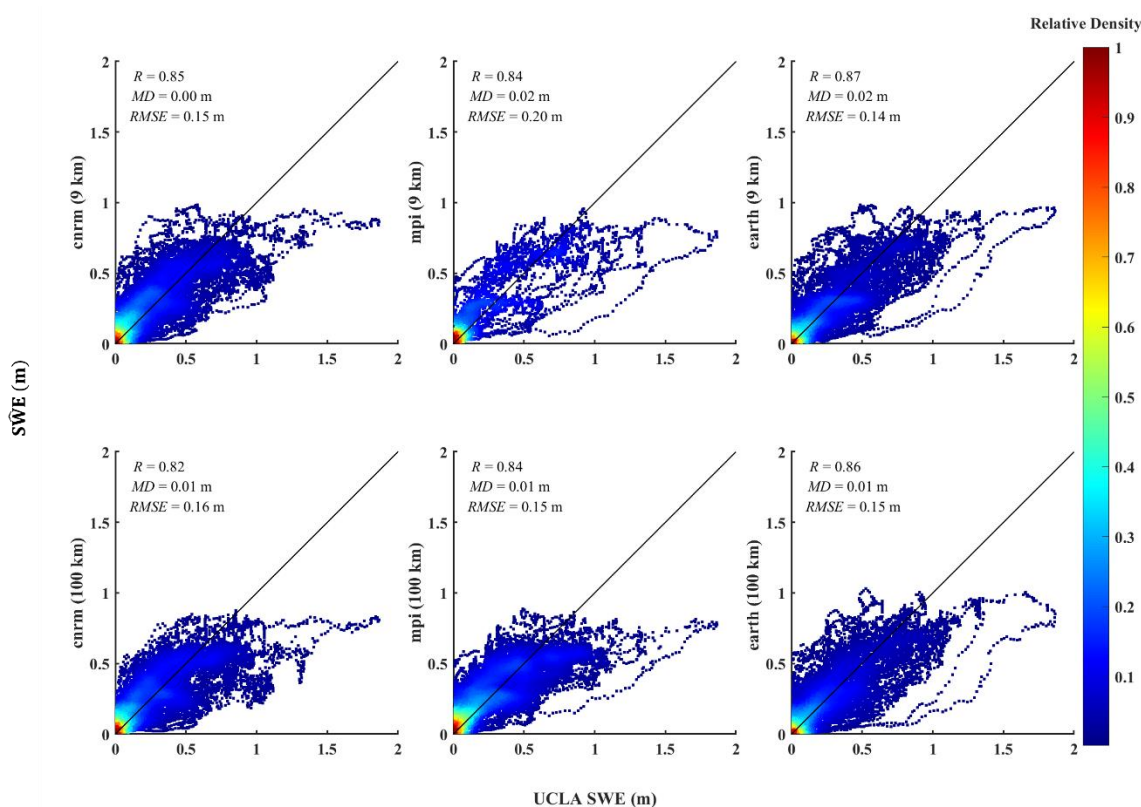
Fig. 5. A density scatter plot in California from 2005 to 2010 compares in-situ data locations (Table 4) from UCLA SWE images to the downscaled SWE (SŴE) values. The solid black line represents the 1:1 line. The displayed metrics include the correlation coefficient (R), mean difference (MD), and Root-Mean-Squared Error (RMSE). Only data with SWE values greater than 1 cm are included in the comparison.

Fig. 6 presents a comparison of the mean SŴE and mean UCLA SWE over a six-year period in California and Colorado. Among the models, the 'cnrm-esm2-1' at 100 km resolution, in most months, outperforms 'ec-earth3-veg' and 'mpi-esm1-2' in

310   Colorado. In contrast, in California, 'ec-earth3-veg' mostly exhibits superior performance at both 9 km and 100 km resolutions.

15

Collectively, these findings emphasize the significance of selecting an appropriate model and its optimal resolution for SWE estimation.
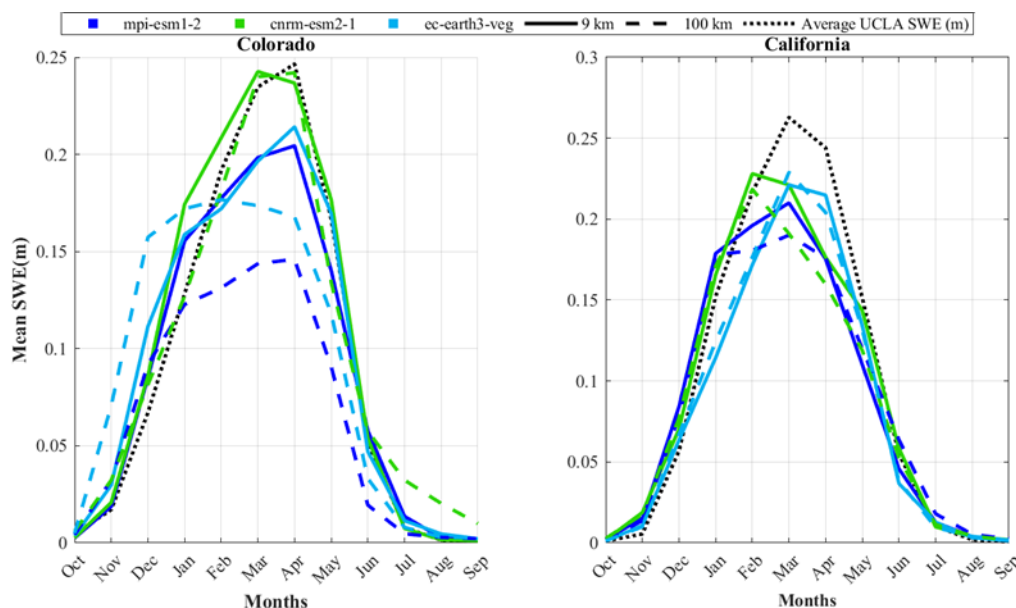

Fig. 6. The average of the UCLA SWE (black dotted line, reference) and downscaled SWE (SŴE; blue and green lines) for each area over the six-year period from 2005 to 2010. For each climate model, SŴE is represented by a unique color: light blue when 'ec-earth3-veg' is used as an estimator, green for 'cnrm-esm2-1', and dark blue for 'mpi-esm1-2'. Within each color group, line styles differentiate the climate data spatial resolutions: solid lines indicate results based on 9 km climate estimators, and dashed lines represent results based on 100 km climate estimators.

Additionally, two videos (one for each study region) have been created to showcase a side-by-side comparison of UCLA SWE and SŴE images for corresponding dates: California (SŴE obtained from 'ec-earth3-veg' at 100 km), Colorado (SŴE obtained from 'cnrm-esm2-1'at 9 km).

5.2 Cross-validation

Cross-validation accuracy assessments of SŴE are outlined in Supplementary Tables S2 and S3. Fig. 7 and 8, and Figs. S9 and S10 in the supplementary material further present these assessments considering variations in elevation and land cover for California and Colorado. Overall, for most months, using climate data with a higher resolution (9 km) as an estimator yields only slightly higher or identical accuracies compared to climate data with a lower resolution (100 km). In a broad comparison across resolutions in Colorado and California, the 'cnrm-esm2-1' and 'ec-earth3-veg' models generally exhibit the best performance. Nonetheless, it is crucial to recognize the variability in model performance across different regions. For instance, in both California and Colorado, all models generally exhibit better or close performance at higher elevations (elevation > 3000 m) compared to medium elevations (2000 m < elevation < 3000 m). Although errors at lower elevations (elevation < 2000 m) are less than at higher elevations, the number of pixels with elevations less than 2000 m is also fewer. This is

16

significant because accurately obtaining snow data at higher elevations is more critical than at other elevations in certain studies

and regions, such as water management for areas where, in summer, most of the water supply originates from higher elevations.

In Colorado, all models exhibit comparable performance in both forested and non-forested areas. In contrast, in California,

models tend to perform slightly better in non-forested areas. Moreover, Fig. 8 and S10 illustrate the average spatial error in

330 March and May, respectively, for California and Colorado. In California, the $\widehat{SWE}$ underestimates reference SWE, with the

extent of underestimation varying across different climate models. For instance, in California, 'cnrm-esm2-1' at 9 km achieves

the lowest underestimation. In general, the 'cnrm-esm2-1' model at 9 km exhibits superior performance for Colorado as an

estimator, with a mean RMSE of 0.06 m and a standard deviation of 0.04 m. Conversely, for California, the 'ec-earth3-veg'

model at 9 km demonstrates the best accuracy as an estimator, yielding a mean RMSE of 0.13 m and a standard deviation of
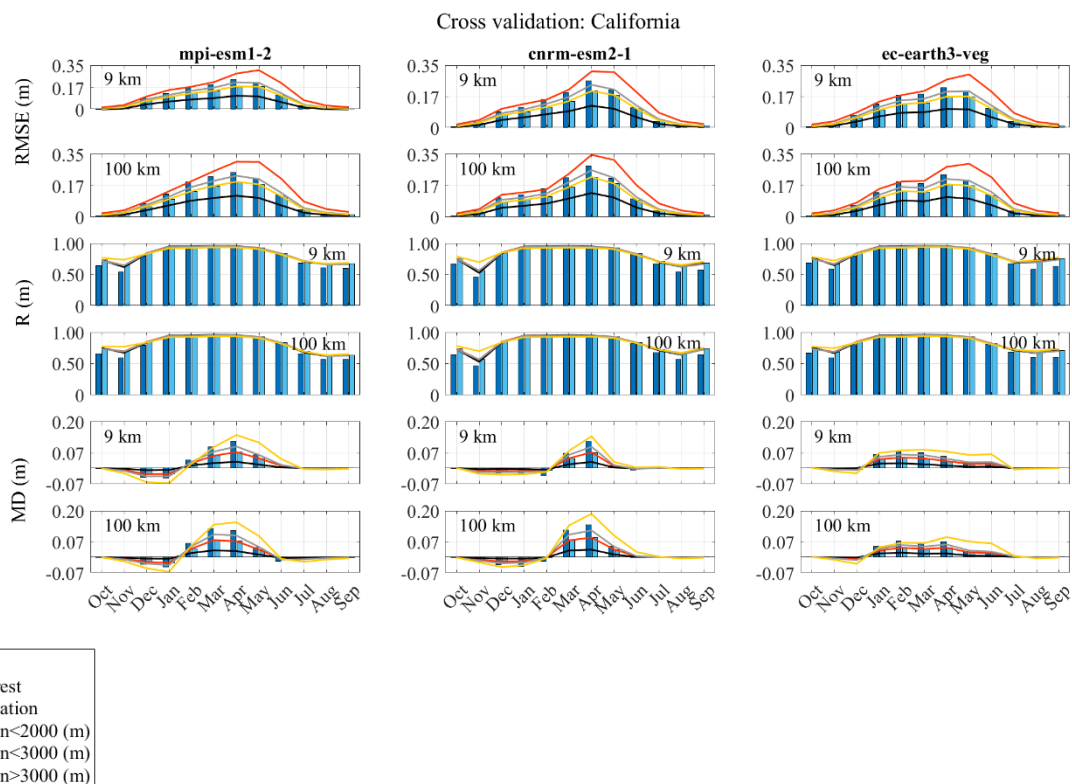
335 0.09 m.

Fig. 7. Accuracy assessment of downscaling cross-validation, conducted in California, over the six-year period from 2005 to 2010. Column titles indicate the results for downscaled SWE ($\widehat{SWE}$) using respective climate models as estimators. '9 km' and '100 km' refer to the resolutions of the climate data. The evaluation metrics include the Correlation Coefficient (R), Mean Difference (MD), and Root-Mean-Squared Error (RMSE). These metrics are considered in different elevation values and different land covers. In the legend, 2000 m <Elevation< 3000 m is shown as Elevation< 3000 m.
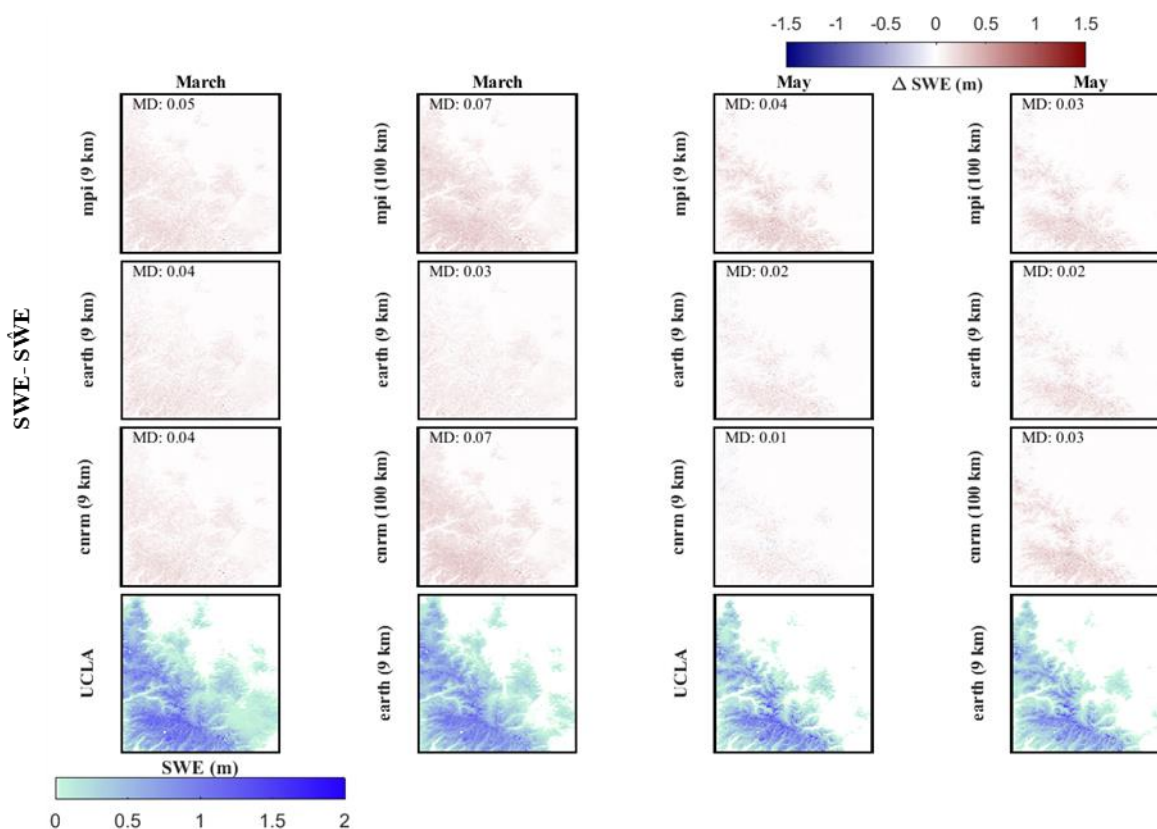
Fig. 8. Spatial assessment of the downscaling. The first three rows represent the mean difference between UCLA SWE and downscaled SWE (SWE- SŴE) over California throughout the 6-year testing period (2005-2010) for two different months (March and May). The last row represents the averaged reference SWE (UCLA SWE) or averaged downscaled SWE (SŴE) throughout the 6-year testing period (2005-2010) for two different months (March and May). The evaluation metric includes Mean Difference (MD).

5.3 Comparison with 1 km SWE SNODAS Dataset

The comparison of UCLA SWE and SŴE with the 1 km resolution SNODAS dataset is detailed in Supplementary Table S4, Figs. 9 and 10, and Figs. S11 and S12. The results align with previous sections: all models exhibit comparable accuracy and correlation levels with the SNODAS SWE data, with distinctions arising based on resolutions, elevation ranges, and land cover

340 types.

In California, during the snowiest months, the 'ec-earth3-veg' estimator excels in terms of RMSE, correlation, and mean difference at both resolutions. In Colorado, the 'mpi-esm1-2' estimator mostly demonstrates superior performance. Interestingly, in Colorado, the 100 km resolution slightly outperforms the 9 km resolution across some models. However, in

some other models, the 100 km is marginally surpassed by the 9 km resolution. In other words, the performance of different

345 resolutions is nearly similar across all models, suggesting that using the coarse-scale CMIP6 resolution can yield results

comparable to those of finer resolutions. According to Fig. 10 and S12 generally, in California, the 'ec-earth3-veg' model

outperforms others at both 9 km and 100 km resolutions in both March and May, although it tends to mostly underestimate the

SWE. In contrast, in Colorado, the 'mpi-esm1-2' model at 9 km performs better in March and May, mostly with an

overestimation tendency. In general, in Colorado, the 'mpi-esm1-2' model at 100 km showed the most favorable results, with

350 a mean RMSE of 0.08 m and a standard deviation of 0.07 m. In California, the 'ec-earth3-veg' model at 9 km outperformed

others, with a mean RMSE of 0.23 m and a standard deviation of 0.20 m.
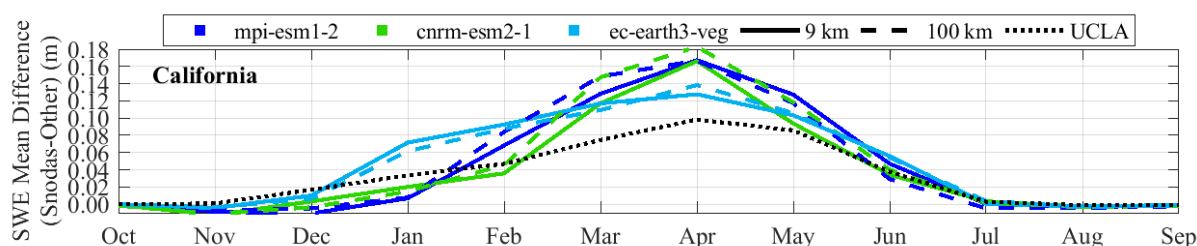
Fig. 9. The average mean difference of SWE over California for the 6-year testing period (2005-2010) compares UCLA SWE (black dotted line) and downscaled SWE (SŴE) data (blue and green lines) against SNODAS. The SŴE data, derived from various climate estimators, are identified in the legend by their names and associated colors: light blue for 'ec-earth3-veg', green for 'cnrm-esm2-1', and dark blue for 'mpi-esm1-2'. Within each color group, line styles distinguish the spatial resolutions of the climate data: solid lines indicate climate estimators at a 9 km resolution, while dashed lines represent climate estimators at a 100 km resolution.
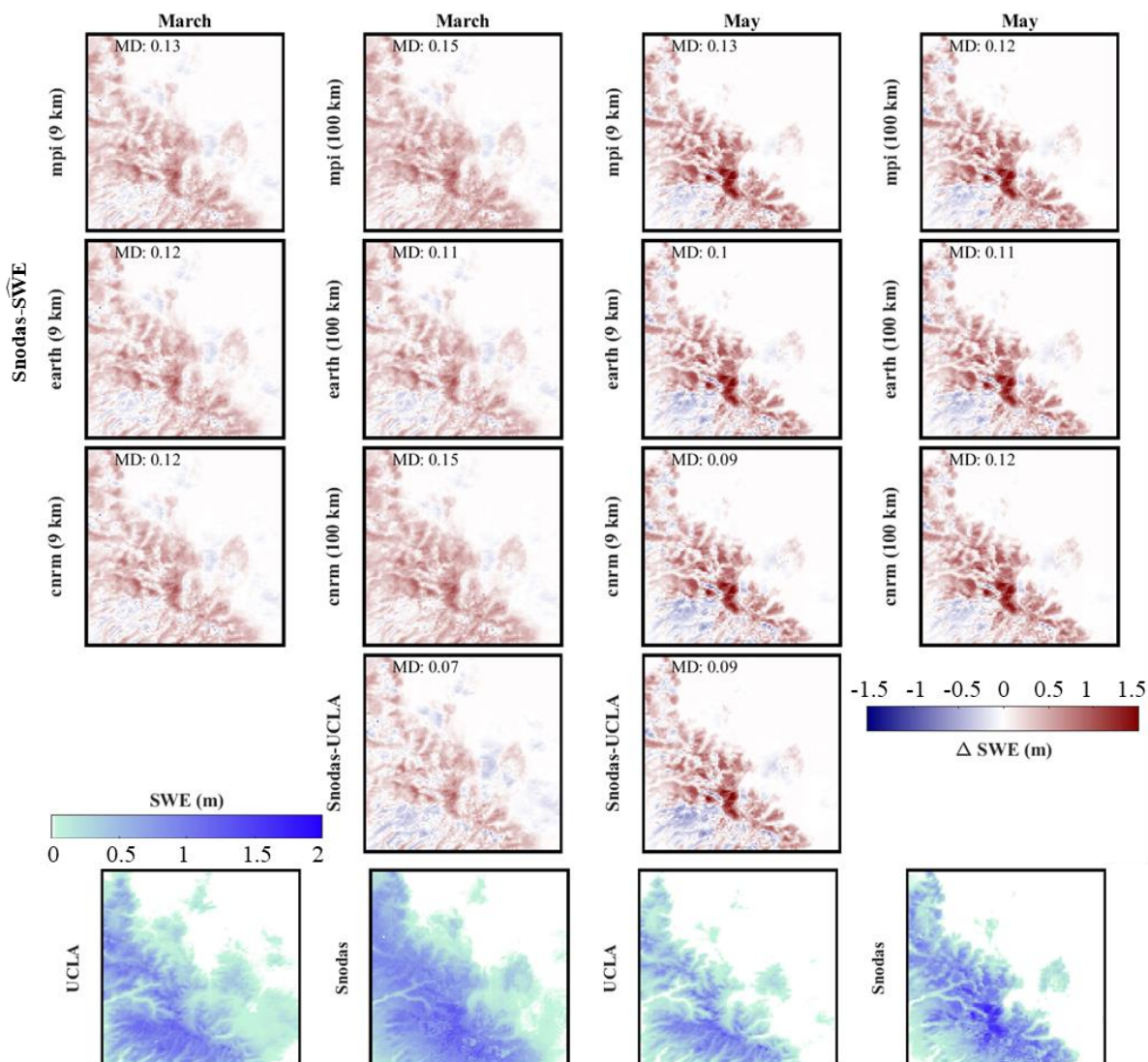
19

Fig. 10. Comparison with SNODAS data. The first four rows present the average difference between SNODAS and downscaled SWE (SŴE) or UCLA SWE (SNODAS- SŴE or SNODAS-UCLA) over California for March and May during the 6-year testing period (2005-2010). The last row compares the average UCLA SWE or SNODAS SWE over California for March and May during the same 6-year testing period (2005-2010). The evaluation metric includes Mean Difference (MD).

5.4 Comparison with 1 km SWE Daymet Dataset

This section presents a comparison of SŴE from three climate models with the 1 km SWE data from the Daymet dataset.

355 Supplementary Table S5, along with, Figs. 11 and 12, and Figs. S13 and S14, showcase the comparison of UCLA SWE and

SŴE against the 1 km SWE Daymet dataset. The results show that all three models display comparable levels of accuracy and correlation with the Daymet SWE data.

In California, the 'ec-earth3-veg' model leads in performance at both 9 km and 100 km resolutions, boasting the lowest RMSE, and highest correlation. For Colorado, the 'cnrm-esm2-1' estimator predominantly demonstrates superior performance. When comparing both the UCLA SWE and SŴE to the 1 km SWE Daymet dataset, the results also indicate a close alignment between the two sets of data. Fig. 12 and S13 demonstrate that in California and Colorado during the months of March and May, the 'cnrm-esm2-1' estimator yields the best results. In both regions, this model predominantly overestimates SWE in March and underestimates it in May. In general, the 'cnrm-esm2-1' estimator at 100 km is the most accurate for Colorado, presenting a mean RMSE of 0.11 m and a standard deviation of 0.04 m. For California, the 'mpi-esm1-2' model at 100 km achieves the best performance, with a mean RMSE of 0.19 m and a standard deviation of 0.06 m. However, 'ec-earth3-veg' achieves the same mean RMSE, with a standard deviation of 0.07 m.
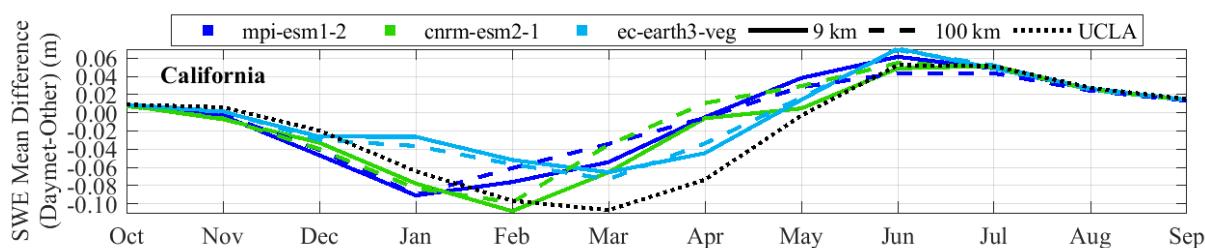

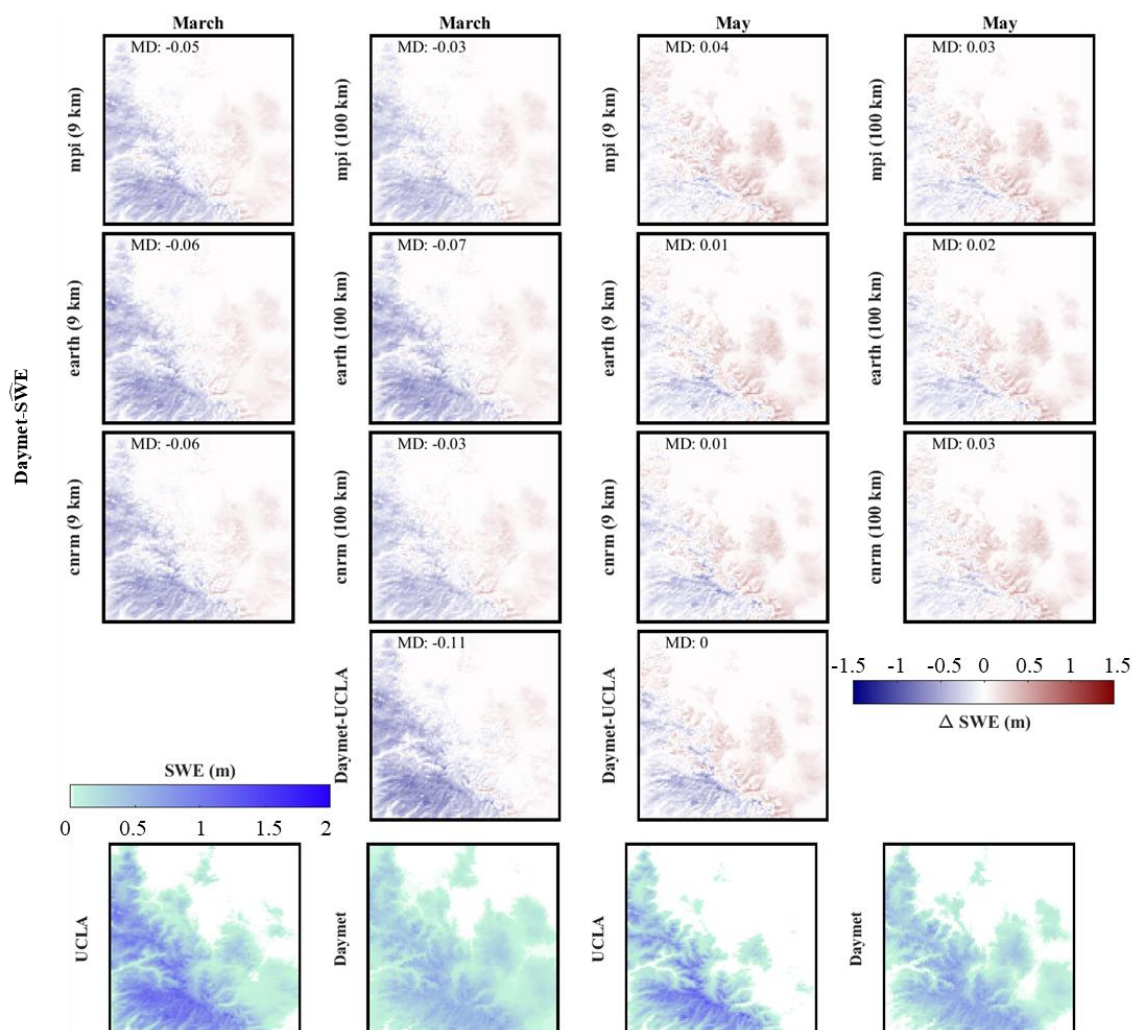**Fig. 11. Same as Fig. 9, but for comparison against the Daymet data.**

Fig. 12. Same as Fig. 10, but for comparison against the Daymet data.

5.5 Comparison with 4 km SWE of the University of Arizona Dataset

This section compares the SŴE from three models against the 4 km SWE data from the University of Arizona (UA).
370 Supplementary Table S6, Figs. 13 and 14, and Figs. S14 and S15 illustrate the comparison between UCLA SWE and SŴE against the 4 km SWE data from the UA dataset. The findings indicate that all three models provide comparable accuracy and correlation with the UCLA SWE, underscoring the effectiveness and reliability of our estimation approach in representing SWE in both California and Colorado.

22

A deeper analysis of model performance reveals subtle differences. In Colorado, the 'cnrm-esm2-1' estimator stands out at both
9 km and 100 km resolutions. Meanwhile, in California, mostly the 'ec-earth3-veg' model surpasses its counterparts, achieving
the lowest mean RMSE at both resolutions.

Overall, the 9 km resolution models slightly outperform the 100 km resolution models in both states. This suggests that a finer
resolution might yield slightly more precise $\hat{\text{SWE}}$ estimates. Additionally, when comparing both the UCLA SWE and $\hat{\text{SWE}}$ to
the 4 km UA SWE, the results demonstrate a tight congruence between the two datasets. Furthermore, Fig. 14 and S15 show
that in California, for March and May, the 'ec-earth3-veg' model at a 100 km resolution performs optimally. Meanwhile, in
Colorado, the 'cnrm-esm2-1' estimator achieves the best performance in these two months. The 'ec-earth3-veg' model tends to
underestimate SWE in California, while in Colorado, 'cnrm-esm2-1' generally overestimates SWE in May. In general, the
'cnrm-esm2-1' estimator at the 9 km scale provides the best results for Colorado, having a mean RMSE of 0.07 m and a standard
deviation of 0.05 m. In California, the 'ec-earth3-veg' estimator at the 9 km scale proves to be the most precise, with a mean
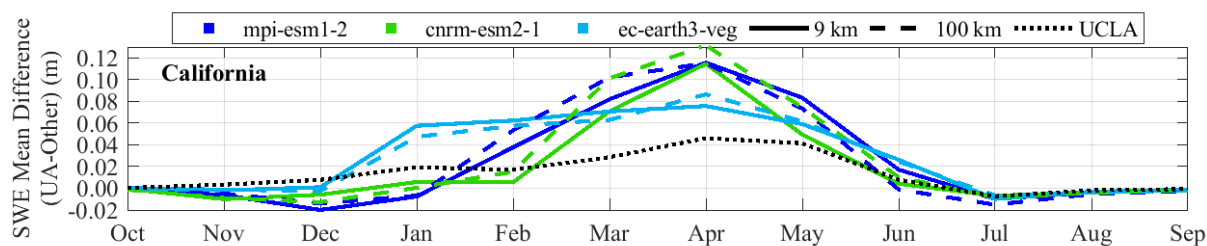RMSE of 0.14 m and a standard deviation of 0.13 m.

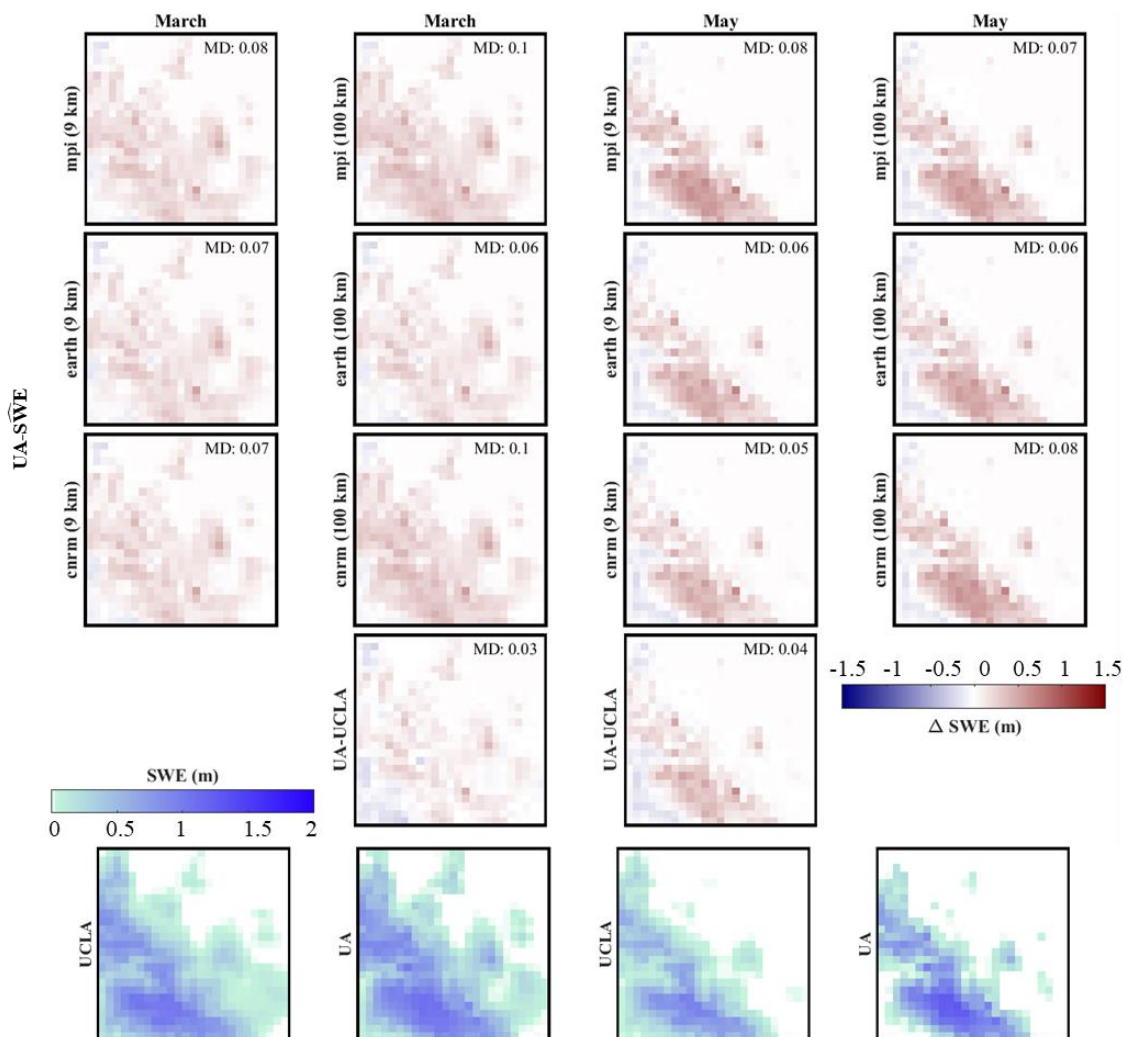**Fig. 13. Same as Fig. 9, but for comparison against the University of Arizona (UA) data.**

Fig. 14. Same as Fig. 10, but for comparison against the University of Arizona (UA) data.

6. Discussion and Conclusion

This research aims to propose a methodology to downscale low-resolution daily Snow Water Equivalent (LR-SWE) by
utilizing low-resolution daily climate data to produce daily, high-resolution SWE (HR-SWE) data, covering the period from
1950 to the present. We test our approach in two distinct areas (California and Colorado) in the western United States. Utilizing
existing low-resolution meteorological factors obtained from global CMIP6 climate data (100 km) and downscaled CMIP6 for
the Western United States (WRF-CMIP6, 9 km) and available 500-meter HR-SWE images from 1984 to 2021 (UCLA SWE
dataset) for the Western United States, we implement a downscaling algorithm to estimate HR-SWE images. WRF-CMIP6 is

24

395 a regional configuration of a climate model that dynamically downscales CMIP6 data, incorporating ERA5 reanalysis data to enhance spatial and temporal resolution. Utilizing both CMIP6 and WRF-CMIP6 at different resolutions allows us to investigate the effects of using a regional climate model that dynamically downscales CMIP6 data and incorporates reanalysis data, alongside a global climate model with different spatial resolutions, on the accuracy of our approach. We also select three climate models ('ec-earth3-veg', 'mpi-esm1-2', and 'cnrm-esm2-1') for testing the proposed method using different models.

400 To perform a comprehensive accuracy assessment, we compared the downscaled SWE ($\hat{SWE}$) with established datasets like the 1 km SWE Daymet, 1 km SWE SNODAS, and the 4 km SWE from the University of Arizona. Moreover, we performed cross-validation accuracy assessments. Our $\hat{SWE}$ data closely mirrored reference HR-SWE conditions. Even when utilizing lower-resolution climate datasets like CMIP6 (100 km), the method remained robust, leveraging recurring SWE patterns and climate data to generate more detailed SWE images.

405 A comprehensive analysis over all months reveals notable patterns in the performance of various climate models at different resolutions in California and Colorado. In general, using the 'cnrm-esm2-1' model as an estimator results in better accuracy in Colorado at both 100 km and 9 km resolutions compared to using other models. This performance highlights the model's strong compatibility with the climatic and geographical complexities of Colorado. Conversely, in California, the 'ec-earth3-veg' model excels at a 9 km resolution, offering the most accurate results. This suggests that its higher resolution better captures the state's

410 complex environmental and topographical variations. It also appeared that a finer resolution of 9 km provided slightly better accuracy than a 100 km resolution across all models, although the difference was not substantial. This underscores the importance of selecting the appropriate climate model for SWE estimation, which can have a more significant impact than merely choosing a higher-resolution model. Moreover, CMIP6 models are designed for long-term climate projections and capture broad climate trends rather than predicting specific weather events. Despite this, the downscaled SWE using the

415 proposed approach based on CMIP6 is comparable to that of WRF-CMIP6, which dynamically downscales CMIP6 data with the incorporation of ERA5 reanalysis data. This is largely because the proposed methodology relies on long-term climate data, and CMIP6 effectively captures broad climatic trends and seasonality, including changes in temperature and precipitation patterns.

 Ongoing research will focus on applying our downscaling framework to predict high-resolution SWE based on future climate

420 predictions. The data generated could be invaluable not only in climate change studies but also for water resources management. This underscores the need for precise model selection and the potential for applying our findings to future climate scenarios, enhancing our understanding and management of water resources in the face of climate change. Moreover, we anticipate that our approach could be applied in areas lacking high-resolution climate models.

Code and Data Availability

The code for generating downscaled SWE maps, along with some sample data, is available in the assets section.

Video Supplement

The videos of High-Resolution SWE estimations for California and Colorado are available in the assets section

Supplement Link

430 It is uploaded while submitting, and the link to the supplement will be included by Copernicus.

Author Contribution

FZ: Conceptualization, Methodology, Software, Validation, Investigation, Data curation, Formal analysis, Writing – original draft.

GM and MG: Conceptualization, Methodology, Validation, Formal analysis, Writing – review & editing, Supervision, Project
435 administration, and Resources.

FZ and GM: Funding acquisition.

Competing Interests

The authors declare that they have no conflict of interest.

Acknowledgments

References

450   U.S. Bureau of Reclamation (USBR): Emerging Technologies in Snow Monitoring, Report to Congress, 2021.

Abatzoglou, J. T.: Development of gridded surface meteorological data for ecological applications and modelling, International
Journal of Climatology, 33, 121-131, 2013.

Abatzoglou, J. T. and Brown, T. J.: A comparison of statistical downscaling methods suited for wildfire applications,
International journal of climatology, 32, 772-780, 2012.

455   Bair, E. H., Rittger, K., Davis, R. E., Painter, T. H., and Dozier, J.: Validating reconstruction of snow water equivalent in
California's Sierra Nevada using measurements from the NASA Airborne Snow Observatory, Water Resources Research, 52,
8437-8460, 2016.

Bales, R. C., Molotch, N. P., Painter, T. H., Dettinger, M. D., Rice, R., and Dozier, J.: Mountain hydrology of the western
United States, Water Resources Research, 42, 2006.

460   Broxton, P., Zeng, X., and Dawson, N.: Daily 4 km Gridded SWE and Snow Depth from Assimilated In-Situ and Modeled
Data over the Conterminous US, Version 1 [Data Set]. Boulder, Colorado USA. NASA National Snow and Ice Data Center
Distributed Active [dataset], 2019.

Center, N. O. H. R. S.: Snow Data Assimilation System (SNODAS) Data Products at NSIDC, Version 1, National Snow and
Ice Data Center, Boulder, Colorado USA2004.

465   Clow, D. W., Nanus, L., Verdin, K. L., and Schmidt, J.: Evaluation of SNODAS snow depth and snow water equivalent
estimates for the Colorado Rocky Mountains, USA, Hydrological Processes, 26, 2583-2591, 2012.

Council, N. R. and Committee, N. W. S. M.: Future of the National Weather Service Cooperative Observer Network, National
Academies Press1998.

Dawadi, S. and Ahmad, S.: Changing climatic conditions in the Colorado River Basin: Implications for water resources
470   management, Journal of Hydrology, 430, 127-141, 2012.

Dietz, A. J., Wohner, C., and Kuenzer, C.: European Snow Cover Characteristics between 2000 and 2011 Derived from
Improved MODIS Daily Snow Cover Products, Remote Sensing, 4, 2432-2454, 10.3390/rs4082432, 2012.

Fang, Y., Liu, Y., and Margulis, S. A.: A western United States snow reanalysis dataset over the Landsat era from water years
1985 to 2021, Scientific Data, 9, 677, 2022.

475   Farr, T. G., Rosen, P. A., Caro, E., Crippen, R., Duren, R., Hensley, S., Kobrick, M., Paller, M., Rodriguez, E., and Roth, L.:
The shuttle radar topography mission, Reviews of geophysics, 45, 2007.

Fleming, S. W., Zukiewicz, L., Strobel, M. L., Hofman, H., and Goodbody, A. G.: SNOTEL, the Soil Climate Analysis Network, and water supply forecasting at the Natural Resources Conservation Service: Past, present, and future, JAWRA Journal of the American Water Resources Association, 2023.

480   Girotto, M., Musselman, K. N., and Essery, R. L.: Data assimilation improves estimates of climate-sensitive seasonal snow, Current Climate Change Reports, 6, 81-94, 2020.

Henn, B., Musselman, K. N., Lestak, L., Ralph, F. M., and Molotch, N. P.: Extreme runoff generation from atmospheric river driven snowmelt during the 2017 Oroville Dam spillways incident, Geophysical Research Letters, 47, e2020GL088189, 2020.

Henson, R.: Flow Cytometry Data Reader and Visualization, MATLAB Central File Exchange [code], 2024.

485   Kouki, K., Räisänen, P., Luojus, K., Luomaranta, A., and Riihelä, A.: Evaluation of Northern Hemisphere snow water equivalent in CMIP6 models during 1982–2014, The Cryosphere, 16, 1007-1030, 2022.

Largeron, C., Dumont, M., Morin, S., Boone, A., Lafaysse, M., Metref, S., Cosme, E., Jonas, T., Winstral, A., and Margulis, S. A.: Toward Snow Cover Estimation in Mountainous Areas Using Modern Data Assimilation Methods: A Review, Frontiers in Earth Science, 8, 10.3389/feart.2020.00325, 2020.

490   Lievens, H., Demuzere, M., Marshall, H. P., Reichle, R. H., Brucker, L., Brangers, I., de Rosnay, P., Dumont, M., Girotto, M., Immerzeel, W. W., Jonas, T., Kim, E. J., Koch, I., Marty, C., Saloranta, T., Schober, J., and De Lannoy, G. J. M.: Snow depth variability in the Northern Hemisphere mountains observed from space, Nature Communications, 10, 10.1038/s41467-019-12566-y, 2019.

Lundquist, J. D., Chickadel, C., Cristea, N., Currier, W. R., Henn, B., Keenan, E., and Dozier, J.: Separating snow and forest
495   temperatures with thermal infrared remote sensing, Remote Sensing of Environment, 209, 764-779, 10.1016/j.rse.2018.03.001, 2018.

Ma, X., Li, D., Fang, Y., Margulis, S. A., and Lettenmaier, D. P.: Estimating spatiotemporally continuous snow water equivalent from intermittent satellite observations: an evaluation using synthetic data, Hydrology Earth System Sciences, 27, 21-38, 2023.

500   Margulis, S. A., Cortés, G., Girotto, M., and Durand, M.: A Landsat-era Sierra Nevada snow reanalysis (1985–2015), Journal of Hydrometeorology, 17, 1203-1221, 2016.

Meehl, G. A., Moss, R., Taylor, K. E., Eyring, V., Stouffer, R. J., Bony, S., and Stevens, B.: Climate model intercomparisons: Preparing for the next phase, Eos, Transactions American Geophysical Union, 95, 77-78: The data was downloaded in January 2023., 2014.

505   Painter, T. H., Bryant, A. C., and Skiles, S. M.: Radiative forcing by light absorbing impurities in snow from MODIS surface reflectance data, Geophysical Research Letters, 39, 10.1029/2012gl052457, 2012.

Pflug, J. and Lundquist, J.: Inferring distributed snow depth by leveraging snow pattern repeatability: Investigation using 47 lidar observations in the Tuolumne watershed, Sierra Nevada, California, Water Resources Research, 56, e2020WR027243, 2020.

510   Pflug, J. M., Wrzesien, M. L., Kumar, S. V., Cho, E., Arsenault, K. R., Houser, P. R., and Vuyovich, C. M.: Extending the utility of space-borne snow water equivalent observations over vegetated areas with data assimilation, Hydrology Earth System Sciences, 28, 631-648, 2024.

Rahimi, S., Krantz, W., Lin, Y. H., Bass, B., Goldenson, N., Hall, A., Lebo, Z. J., and Norris, J.: Evaluation of a Reanalysis-Driven Configuration of WRF4 Over the Western United States From 1980 to 2020, Journal of Geophysical Research:

515   Atmospheres, 127, e2021JD035699, 2022.

Rahimi, S., Huang, L., Norris, J., Hall, A., Goldenson, N., Krantz, W., Bass, B., Thackeray, C., Lin, H., and Chen, D.: An overview of the Western United States Dynamically Downscaled Dataset (WUS-D3), Geoscientific Model Development, 17, 2265-2286, 2024.

Ranzi, R., Colosio, P., and Galeati, G.: Climatology of snow depth and water equivalent measurements in the Italian Alps

520   (1967–2020), Hydrology Earth System Sciences, 28, 2555-2578, 2024.

Rettie, F. M., Gayler, S., Weber, T. K., Tesfaye, K., and Streck, T.: High-resolution CMIP6 climate projections for Ethiopia using the gridded statistical downscaling method, Scientific data, 10, 442, 2023.

Saberi, N., Kelly, R., Flemming, M., and Li, Q.: Review of snow water equivalent retrieval methods using spaceborne passive microwave radiometry, International Journal of Remote Sensing, 41, 996-1018, 2020.

525   Shahriari, B., Swersky, K., Wang, Z., Adams, R. P., and De Freitas, N.: Taking the human out of the loop: A review of Bayesian optimization, Proceedings of the IEEE, 104, 148-175, 2015.

Shi, J. and Dozier, J.: Inferring snow wetness using C-band data from SIR-C's polarimetric synthetic aperture radar, IEEE transactions on geoscience remote sensing, 33, 905-914, 1995.

Shi, J. and Dozier, J.: Estimation of snow water equivalence using SIR-C/X-SAR. II. Inferring snow depth and particle size,

530   IEEE Transactions on Geoscience Remote sensing, 38, 2475-2488, 2000.

Siirila-Woodburn, E. R., Rhoades, A. M., Hatchett, B. J., Huning, L. S., Szinai, J., Tague, C., Nico, P. S., Feldman, D. R., Jones, A. D., and Collins, W. D.: A low-to-no snow future and its impacts on water resources in the western United States, Nature Reviews Earth and Environmental, 2, 800-819, 2021.

Snapir, B., Momblanch, A., Jain, S., Waine, T. W., and Holman, I. P.: A method for monthly mapping of wet and dry snow

535   using Sentinel-1 and MODIS: Application to a Himalayan river basin, International Journal of Applied Earth Observation Geoinformation, 74, 222-230, 2019.

Snoek, J., Larochelle, H., and Adams, R. P.: Practical bayesian optimization of machine learning algorithms, Advances in neural information processing systems, 25, 2012.

Sturm, M., Goldstein, M. A., and Parr, C.: Water and life from snow: A trillion dollar science question, Water Resources

540   Research, 53, 3534-3544, 2017.

Tabari, H., Paz, S. M., Buekenhout, D., and Willems, P.: Comparison of statistical downscaling methods for climate change impact analysis on precipitation-driven drought, Hydrology Earth System Sciences, 25, 3493-3517, 2021.

Thornton, M., Shrestha, R., Wei, Y., Thornton, P., Kao, S., and Wilson, B.: Daymet: daily surface weather data on a 1-km grid for North America, Version 4 R1. ORNL DAAC, Oak Ridge, Tennessee, USA, https://doi.org/10.3334/ORNLDAAC/2129 , 2022.

545 2022.

Thrasher, B., Wang, W., Michaelis, A., Melton, F., Lee, T., and Nemani, R.: NASA global daily downscaled projections, CMIP6, Scientific data, 9, 262, 2022.

Tsang, L., Durand, M., Derksen, C., Barros, A. P., Kang, D.-H., Lievens, H., Marshall, H.-P., Zhu, J., Johnson, J., and King, J.: Global Monitoring of Snow Water Equivalent using High Frequency Radar Remote Sensing, The Cryosphere Discussions,

550 2021, 1-57, 2021.

Wu, X., Naegeli, K., Premier, V., Marin, C., Ma, D., Wang, J., and Wunderle, S.: Evaluation of snow extent time series derived from Advanced Very High Resolution Radiometer global area coverage data (1982–2018) in the Hindu Kush Himalayas, The Cryosphere, 15, 4261-4279, 2021.

Wundram, D. and Löffler, J.: High-resolution spatial analysis of mountain landscapes using a low-altitude remote sensing

555 approach, International Journal of Remote Sensing, 29, 961-974, 2008.

Zakeri, F. and Mariethoz, G.: Synthesizing long-term satellite imagery consistent with climate data: Application to daily snow cover, Remote Sensing of Environment, 300, 113877, 2024.

Zeng, X., Broxton, P., and Dawson, N.: Snowpack change from 1982 to 2016 over conterminous United States, Geophysical Research Letters, 45, 12,940-912,947, 2018.

560